# Nanoscale morphology and indentation of individual nacre tablets from the gastropod mollusc *Trochus niloticus*

B.J.F. Bruet
*Department of Materials Science and Engineering, Massachusetts Institute of Technology, Cambridge, Massachusetts 02139*

H.J. Qi[a] and M.C. Boyce
*Department of Mechanical Engineering, Massachusetts Institute of Technology, Cambridge, Massachusetts 02139*

R. Panas, K. Tai, L. Frick, and C. Ortiz[b]
*Department of Materials Science and Engineering, Massachusetts Institute of Technology, Cambridge, Massachusetts 02139*

(Received 27 January 2005; accepted 2 May 2005)

The inner nacreous layer of gastropod mollusc *Trochus niloticus* is composed of ~95 wt% planar arrays of polygonal aragonite-based tablets (~8 μm wide, ~0.9 μm thick, stacked ~40 nm apart) and ~5 wt% biomacromolecules. High-resolution tapping mode atomic force microscope images enabled nanoscale resolution of fractured tablet cross-sections, the organic component, and deformation of individual nanoasperities on top of tablet surfaces. Nanoindentation was performed on individual nacre tablets and the elastic modulus $E$ and yield stress $\sigma_y$ were reduced from elastic-plastic finite element simulations yielding $E = 92$ GPa, $\sigma_y = 11$ GPa (freshly cleaved samples) and $E = 79$ GPa, $\sigma_y = 9$ GPa (artificial seawater soaked samples). Images of the indents revealed extensive plastic deformation with a clear residual indent and surrounding pileup.

## I. INTRODUCTION

Nacre is an extraordinary example of a hierarchical biological nanocomposite and is found in the interior of many mollusc shells.[1,2] Though nacre is composed of exceedingly weak constituent materials, its unique and highly organized design at multiple length scales (Fig. 1) enables outstanding mechanical performance including an excellent combination of stiffness, strength, impact resistance, and toughness.[1,3–6] The structure of nacre has been reviewed previously;[7,8] it is a composite material with a so-called "brick-and-mortar" structure [Fig. 1(a)] consisting of alternating layers of mineral tablets separated by thin layers of a biomacromolecular "glue." Nacre is composed of ~95 wt% pseudo-hexagonal, polygonal, or rounded aragonite tablets (a mineral form of $CaCO_3$, orthorhombic, *Pnma*[9]) which have dimensions of ~5–20 μm (plane with normal defined by the crystallographic *c*[001]-axis) and ~0.3–1.5 μm in thickness (vertically parallel to the *c*[001]-axis)[7,8] as shown in Fig. 1(b). For gastropod nacre, demineralization and scanning electron microscopy imaging suggests that each tablet is subdivided by radial vertical organic membranes into a varying number (2–50) of sectors [Fig. 1(c)], which have been interpreted as polysynthetically twinned crystalline lamellae.[10] The surface of nacre tablets [Fig. 1(d)] from California red abalone (*Haliotis rufescens*) possesses nanoasperities (~30–100 nm diameter and ~10 nm in height)[3,11] and mineral "bridges" [Fig. 1(b)] (~25–34 nm in size, ~91–116 $\mu m^{-2}$ surface density)[12–16] between sheets which pass through the organic intertablet layers. Additionally, even smaller vertical crystalline elements have been mentioned within the nacre tablet lamellae.[17] The organic matrix composes the remaining ~5 wt% of the material [Figs. 1(b) and 1(d)]. The organic matrix of nacre has been studied in a number of reports.[18–31,53] The intertablet polymer layer has a thickness that varies between ~30–300 nm[32] with pores for mineral bridges to pass through,[15] and intracrystalline proteins are present within the tablets themselves.[3,10,33] Lustrin A is one protein that has been isolated from the organic matrix of California red abalone nacre and was found to have a "modular" structure, i.e., a multidomain architecture composed of folded modules (each a few nanometers in size), which are covalently linked together in series along a single macromolecular chain. Lustrin A

[a]Present address: Department of Mechanical Engineering, University of Colorado, Boulder, CO 80309
[b]Address all correspondence to this author.
e-mail: cortiz@mit.edu
DOI: 10.1557/JMR.2005.0273

 © 2005 Materials Research Society

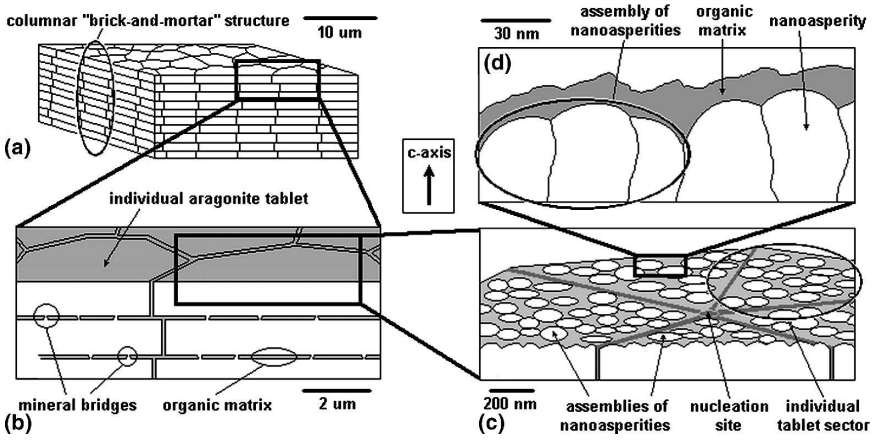


FIG. 1. Schematic illustration of the multiscale hierarchical structure of nacre: (a) 10 μm length scale, (b) 2 μm length scale, (c) individual tablet features at a 200 nm length scale, and (d) 30 nm length scale showing structure of nanoasperities. In "columnar" nacre, the tablets are relatively uniform in size and stacked vertically parallel to the *c*-axis direction (with a slightly staggered arrangement laterally), thereby forming microlaminate sheets and tessellated bands; domain structure has been found parallel to the *c*-axis direction consisting of 3–10 tablets with their *a*-axis parallel to each other, while in the plane of the sheet, the *a*-axis orientation is variable.[57–59]

has approximately ten alternating cysteine and proline-rich domains.[18]

Micro- and macroscopic mechanical testing on nacre has been performed in tension,[1,6] three-point bend,[1,3,6] four-point bend,[3] and indentation.[34] Nacre is anisotropic,[35] exhibits hysteresis on unloading after tensile deformation, and plastically deforms up to fracture strains of ~0.018 in tension.[6] Nacre mechanical property values have been reported as follows: elastic moduli (60–80 GPa[1,3]), tensile, compressive, and three-point bend strengths (35–168,[1,6] 100–540,[4] and 194–248[3] MPa, respectively), modulus of rupture (~270 MPa[36]), three-point bend fracture toughness (2.1–5.0 $MNm^{-3/2}$),[1] and three-point bend work of fracture (150–1650 $Jm^{-2}$),[1,6] depending on the species, orientation of applied load, and degree of hydration. A full understanding of the toughening mechanisms of nacre has not yet been achieved and is an area of great interest and activity. Numerous modes of deformation take place, many of which most likely originate at nanometer-range length scales. For example; rupture of "sacrificial" weaker bonds in the organic component,[53] extension, pull-out, and/or ligament formation of an organic component bridging the tablet interfaces,[1] interacting nanoasperities and mechanical interlocking providing slip resistance and leading to inelastic strain, the formation of periodic dilatation bands between plate edges,[3,37] debonding of mineral-organic interfaces, and tortuous crack propagation due to the microlaminate "tablet and mortar" structure. Continuum mechanical approaches involving three-dimensional finite element analysis (FEA) simulations are now being used to investigate the role of some of these mechanisms such as nanoasperities, mineral bridge contacts, inelastic deformation, and strain hardening.[38] The effectiveness of the organic matrix to shield cracks and influence the toughness of nacre has been studied via a virtual internal bond (VIB) model.[39] Micromechanical models are also starting to be developed, which take into account both the spatial organization of the organic and inorganic components as well as sequential force-induced unfolding of the individual compacted domains in the organic matrix.[40,41]

It has become increasingly evident that knowledge of the fine details of the nanoscale mechanical properties and deformation mechanisms will be critical to the success of such theoretical efforts in their attempt to understand macroscopic mechanical function and performance. Research in this area is just beginning with a few studies recently reported as follows. Nanoindentation experiments up to 200 μN of force on individual thermally etched nacre tablets from California red abalone were found to be minimally hysteretic and exhibited two distinct deformation regimes, which were attributed to initial plastic flattening of surface nanoasperities followed by elastic deformation of the tablet body.[42] The secondary elastic regime data was well described by an analytical solution to a transversely isotropic elastic contact mechanical model[43] using the known elastic constants for aragonite.[35] Another nanoindentation study[11] up to larger forces of ~800 μN on diamond-cut, mechanically ground, polished, and hydrated nacre from California red abalone showed marked hysteresis and fits of these data to an elastic contact mechanical model[44] yielded moduli between ~60 and 80 GPa. Atomic force microscopy (AFM) imaging of the indented regions showed plastic deformation, a pileup height of a few nanometers spanning lateral distances of ~100 nm, and no indication of microcracks.[11]

In this study, we report the nanoscale elastic and plastic indentation properties of individual nacre tablets from the gastropod mollusc *Trochus niloticus* using a sample

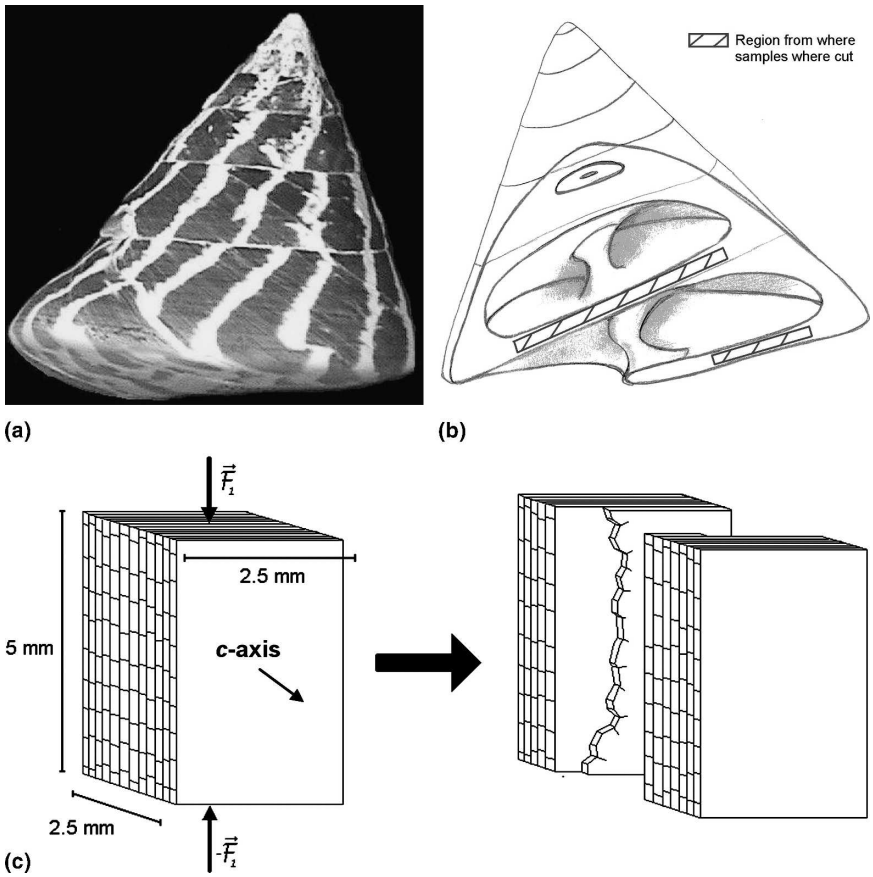


FIG. 2. (a) Photo of *Trochus niloticus* seashell (~6 cm in size), (b) schematic illustration of location where nanoindentation samples were cut from, and (c) schematic illustration of uniaxial compression resulting in cleavage and flat exposed surfaces appropriate for nanoindentation.

preparation methodology involving uniaxial compression with the externally applied load oriented perpendicular to the nacre tablet *c*-axis, producing intertablet cleavage with minimal damage to the individual nacre tablets and an exceedingly flat surface. This sample preparation protocol (which avoided polishing, chemical etching, thermal treatment, and embedding) combined with high-resolution AFM imaging enabled the surface morphology to be studied before and after nanoindentation and, for the first time, shows nanoscale resolution of fractured tablet cross-sections, the conformation of the organic component, and deformation of individual nanoasperities. Another objective of this work was to study the effect of hydration and hence, freshly cleaved samples were compared to ones that had been soaked for 30 days in artificial seawater (0.4221 mol/l NaCl, 0.011 mol/l KCl). The maximum applied forces ranged between ~50–1000 μN, corresponding to indentation depths of ~10–100 nm and a maximum contact area of ~0.1 $\mu m^2$ (corresponding to the projected area of a Berkovich probe tip under load). at a maximum load of 1000 μN. Lastly, a bilayered continuum mechanical elastic-plastic finite element analysis (FEA) model was developed and refined to capture the observed deformation behavior.

## II. MATERIALS AND METHODS

### A. Sample preparation

*Trochus niloticus* shell specimens [~10 cm in size, Fig. 2(a)] were purchased from Shell Horizons (Clearwater, FL). The least destructive, minimum sample preparation procedures possible were used which involved no alcohol dehydration, thermal or chemical treatment, embedding, or polishing. First, nacre from the inner layers of *Trochus niloticus* shells [Fig. 2(b)] were sectioned into parallelepipedal samples using a diamond impregnated annular wafering saw (Buehler, Isomet 5000 Lake Bluff, IL) running at 800–900 rpm. After cutting, the samples were cleaned in reverse osmosis filtrated water for 15 min using an Ultramet ultrasonic cleaner (Pacoima, CA). Samples for nanoindentation, as well as top view (view looking down the aragonite *c*-axis) AFM and scanning electron microscope (SEM) imaging, were produced by uniaxial compression using a Zwick mechanical tester (Model BTC-FR010TH.A50, Kennesaw, GA, 10 kN maximum load cell, 0.01 mm/min, ambient conditions). The externally applied load was oriented perpendicular to the aragonite *c*-axis, producing a clean intertablet cleavage [Fig. 2(c)]. For nanoindentation tests, two types

of samples were used. "Freshly cleaved" samples were tested within less than 1 h after cleaving via uniaxial compression. "Artificial seawater soaked" samples were immersed for 10 weeks in reverse osmosis filtrated water with 0.4221 mol/l NaCl, 0.011 mol/l KCl, pH = 7.1 in a hermetically sealed container at 20 °C, uniaxially compressed, and then tested within less than 1 h after cleaving. Samples for cross-sectional SEM imaging (view perpendicular to the aragonite *c*-axis) were produced by 3-point bend using the same Zwick mechanical tester (0.1 mm/min, ambient conditions) where the externally applied load was oriented parallel to the aragonite *c*-axis.

### B. High-resolution imaging

#### 1. SEM

Samples were coated with 10 nm Au–Pd and imaged using a JEOL SEM 6060 (Peabody, MA) and a JEOL SEM 6320F. The working distances were 6–9 mm (SEM 6060, Peabody, MA) and 12–15 mm (SEM 6320F, Peabody, MA), and the sample plane was oriented perpendicular to the electron beam incidence. A 10–20 kV accelerating voltage was used. Top-view SEM samples were dried in ambient conditions 12 weeks prior to imaging. An environmental SEM (Philips/FEI XL30 FEG SEM, Hillsboro, OR) that allows for low vacuum electron detection in a water vapor environment using uncoated samples (electron acceleration ~15 kV, operating current ~42 μA, working distance ~11 mm, water vapor pressure ~0.4 torr) was also used to produce backscattered electron microscope (BSE) images of freshly cleaved samples.

#### 2. AFM

Contact and tapping mode atomic force microscope (CMAFM and TMAFM, respectively) imaging in ambient conditions were used to produce surface images of freshly cleaved nacre samples. In ambient humidity, a thin layer of water (2–10 Å thick) exists on the surface,[45] yielding images closer to the naturally hydrated state of the shells. A Digital Instruments Multimode SPM IIIA (Veeco, Santa Barbara, CA) was used with AS-130 "JV" or "EV" piezoelectric scanners. Contact mode scans were conducted with Veeco (Santa Barbara, CA) $Si_3N_4$ cantilevers (V-shaped with approximately square pyramidal probe tip geometry, tip half angle ~35°; cantilever length, $l$ ~ 200 μm; nominal spring constant, $k$ ~ 0.32 N/m; and nominal probe tip radius of curvature, $R_{TIP}$ ~ 40 nm). Tapping mode scans were conducted with Veeco Si cantilevers (V-shaped with approximately square pyramidal probe tip geometry, tip half angle of ~17.5°; $l$ ~ 125 μm; $k$ ~ 0.40 N/m; and $R_{TIP}$ ~ 10 nm). A scan rate of 0.25–2 Hz using a maximum sample size of 512 × 512 pixels was used at gains between 0.1 and 0.3. The drive amplitude and amplitude set-point were optimized upon tuning. The $x$ and $y$ scan directions were calibrated with a 10 × 10 $\mu m^2$ grid and the $z$ direction was calibrated with 5 nm diameter beads on a cleaved mica surface. The images to be shown report amplitude (i.e., cantilever oscillation amplitude) and phase (i.e., cantilever phase lag) for tapping mode or deflection for contact mode (i.e., cantilever deflection). Amplitude and deflection both reflect surface topography while phase mode is sensitive to many properties such as friction, adhesion, (visco)elasticity, and composition.

For in-situ imaging of residual indents, a Quesant Q-Scope 350 (attached to a Hysitron, Inc. nanoindentor, Minneapolis, MN) was used in tapping mode with a piezoelectric tube scanning element (X-Y scan range ~40 μm, vertical Z limit ~4.5 μm) and $Si_3N_4$ Wavemode NSC16 cantilevers (rectangular shaped with conical probe tip geometry; $l$ ~ 230 μm; width ~40 μm; cone angle < 20°; probe tip height ~15–20 μm; resonance frequency, ω ~ 170 kHz; $k$ ~ 40 N/m; and $R_{TIP}$ ~ 10 nm). A scan rate of 2 Hz using a maximum sample size of 512 × 512 pixels was used. The drive amplitude and amplitude set-point (~0.25 V) were optimized prior to imaging, and gains between 350 and 550 were used.

Other standard characterization techniques including ash weight, demineralized weight, Raman spectroscopy, x-ray diffraction, and Fourier transform infrared spectroscopy (FTIR) are given in the Appendix.

### C. Nanoindentation

Nanoindentation experiments (Fig. 3) were conducted in ambient conditions using a Hysitron, Inc. (Minneapolis, MN) Triboindenter equipped with TMAFM (Quesant Q-Scope, Agoura Hills, CA) for topographic imaging of residual impressions. The instrument is housed in a granite frame environmental isolation chamber to minimize instabilities due to the ambient background noise, active piezoelectric vibration control stages (Hysitron, Inc.), and a thermal drift calibration step. Load-controlled nanoindentation was performed using a Berkovich (trigonal

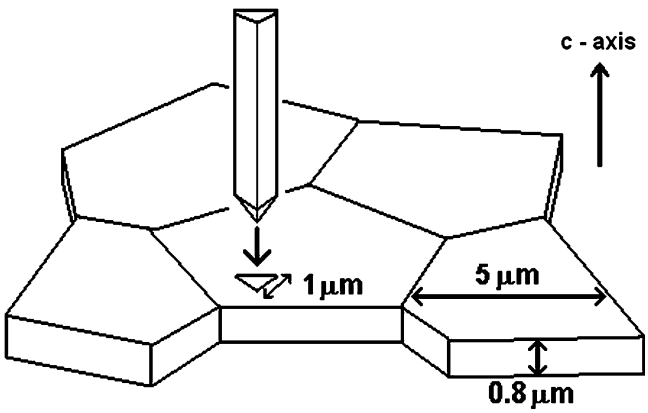


FIG. 3. Schematic illustration of the nanoindentation of an individual nacre tablet.

pyramid) diamond probe tip with the loading axis parallel to the aragonite *c*-axis. The piezoelectric transducer was allowed to equilibrate for 660 s (the last 60 s with digital feedback) prior to each indent. The drift rate of the transducer was automatically monitored by the software before indentation was initiated. The applied load function was divided into five segments as follows. The first segment consisted of a 3 s hold at zero force allowing for tip–sample equilibration. Segment two was a constant loading rate of 10 μN/s. Once the maximum set peak load was reached, a third segment, a hold period of 10 s, would follow. The fourth segment decreases the load until reaching zero force with an unloading rate equivalent to that of segment 2. The fifth segment would conclude the experiment with a 50 s hold at zero force to calculate the final drift rate of the piezo. Maximum loads of 50, 100, 250, 500, 750, and 1000 μN were selected. ~15 experiments per maximum load were performed in a square grid arrangement with each indent spaced 15 μm apart (i.e., thus probing 15 different individual nacre tablets). Load versus indentation distance (depth) curves from multiple experiments using the same maximum load and from different sample locations were averaged and standard deviations calculated and reported. The probe tip area function [$A(h_c)$, which is the projected area of the Berkovich probe tip under load calculated from a 6th order polynominal fit accounting for nonideal tip geometry as a function of the contact depth $h_c$] and frame compliance were calibrated prior to each set of experiments using a fused quartz sample.

### D. Mechanical property approximation from nanoindentation data

The elastic, plastic, and total work of indentations ($W_e$, $W_p$, and $W_T$, respectively) were calculated from the nanoindentation data as follows. $W_e$ was defined as the area under the unloading curve, $W_p$ was defined as the area between the loading and unloading curves (mechanical hysteresis or energy dissipated), and $W_T$ was defined as the area under the loading curve.

Two different approaches were used to approximate the mechanical properties from nanoindentation data. First, the Oliver–Pharr (O-P) methodology,[44] where the initial (95–20%) unloading curve was compared to continuum mechanical theory for an isotropic, elastic half-space where the elastic modulus $E$ was the only fitting parameter. The hardness was calculated as $H = P_{max}/A_{max}$, where $P_{max}$ is the maximum load and $A_{max}$ is the projected area of contact at the maximum contact depth and represents the load-bearing capacity of the material. Unpaired student t-tests[46] were carried out to evaluate whether various datasets were statistically different from each other using $p < 0.05$ as the minimum criterion.

Second, elastic–perfectly plastic FEA simulations were used in which the loading and unloading curves were fit using two material parameters for the nacre tablet, the elastic modulus and the yield stress $\sigma_Y$. Aragonite is known to be orthotropic.[35] Within an individual nacre tablet, random in-plane (perpendicular to the *c*-axis) orientation due to the sector structure is expected, yielding a transversely isotrophic solid at these length scales [Fig. 1(c)]. Simulations were performed taking into account both elastic and plastic anisotropy; this anisotropy was found to have minimal influence (<5%) on the resulting values of the modulus and yield stress. The FEA model was constructed as a two layer material (i.e., the mineral and the organic matrix components) with a stiffer layer representing the 870 nm thick nacre tablet and a 40-nm-thick organic matrix layer. The thickness values were chosen based on SEM measurements. The organic matrix was assumed to behave similar to an elastomer and modeled by the Arruda–Boyce 8-chain model,[47] which has been shown to adeduately capture the stress-strain behavior of rubbers and soft tissues.[48,49] The stress–strain law for the Arruda–Boyce 8-chain model is[47]

$$\mathbf{T} = \frac{1}{J}\,\mu\,\frac{\sqrt{N}}{\lambda}\,L^{-1}\left(\frac{\lambda}{\sqrt{N}}\right)\overline{\mathbf{B}} + K_B\,[J-1]\,\mathbf{I} \quad , \qquad (1)$$

where $\mathbf{T}$ is the Cauchy stress tensor, $\overline{\mathbf{B}}$ is the isochoric deviatoric left Cauchy–Green tensor, $\lambda$ is chain stretch ratio and is defined as the trace of $\overline{\mathbf{B}}$, i.e., $\lambda = tr(\overline{\mathbf{B}})$, $J$ is the volumetric ratio during deformation, $\mathbf{I}$ is a unit tensor, $L^{-1}$ is inverse Langevin function, and $\mu$, $N$, and $K_B$ are material parameters in which $\mu$ is the shear modulus (set equal to 100 MPa), $N$ is the number of the rigid links between crosslink sites in the macromolecule and characterizes molecular chain extensibility (set equal to 10), and $K_B$ is the bulk modulus (set equal to 2 GPa). Among these parameters, $\mu$ has the strongest influence on the material shear stress-strain response at small strains whereas $N$ more heavily influences the large strain behavior. The organic matrix is 870 nm below the indenting surface and laterally confined due to the high stiffness of the mineral tablet. The lateral confinement will make the stress state in the organic layers predominantly (negatively) hydrostatic during these indentation loading conditions; thus the choice of $\mu$ was expected to have a small effect on the overall indentation force versus depth predictions. This was demonstrated by comparing the results from three simulations, where $\mu$ was chosen as 1 GPa, 100 MPa, and 10 MPa, respectively. The resulting difference in indentation force versus penetration responses was <4% (data not shown). $E$ and $\sigma_Y$ of nacre tablet were best fit to capture the experimental data. Forty nanometers was the thickness used for the organic layer (as measured by SEM). The symmetry of the Berkovich indenter enabled simulations using 1/6 of the indenter and the material with appropriate symmetry boundary conditions. Since the elastic modulus of the diamond probe tip

is approximately 10× greater than that of nacre, the indenter was modeled as a rigid surface. Due to fabrication and wear, the Berkovich probe does not possess completely sharp tip geometry; instead it is rounded and can be characterized by a finite probe tip end radius and truncate height (which is defined to be the distance between the apex of the rounded tip and the apex of the imaginary ideally sharp tip). To approximate the probe tip end radius and truncate height, nanoindentation experiments were conducted on a standard fused quartz sample. Hertz contact solution provided an initial estimate and FEA simulations refined this estimate to give more accurate values. Hence, for all FEA simulations, the indenter was modeled as a rigid surface with Berkovich geometry (ideal geometry possesses an inclined face angle $\beta$ of 24.7° and an apex angle $\gamma$ of 77.1°) having a probe tip radius of 300 nm and truncate height of 7 nm. The nacre was modeled using 8-node trilinear hybrid tablet elements (C3D8H in ABAQUS, element library, Providence, RI). The mesh was refined in the vicinity of the contact region where large gradients in stress and strain prevail. Several mesh densities were analyzed, and an optimal mesh was finally chosen for use in all simulations, which contained 6195 nodes and 5491 elements. Large deformation theory and frictionless contact between the indenter and material were assumed throughout the analysis. A smaller number of individual experimental nanoindentation curves were fit ($n = 3$, where the average, high, and low curves were fit for each dataset) and compared to the O-P method due to the longer time and computational cost required for the FEA simulations.

## III. RESULTS

### A. High-resolution imaging: SEM, BSE, and AFM

#### 1. SEM

Figure 4(a) shows SEM images of a nacre sample fractured in 3-point bending (aragonite *c*-axis orientation is vertical) and reveals a regular microstructure consisting of planes of tablets stacked in the aragonite *c*-axis direction where the tablets are staggered with respect to one another from plane to plane; the left image is approximately the same length scale as the schematic shown in Fig. 1(a), and the right image is approximately the same length scale as the schematic shown in Fig. 1(b). Figure 4(b) shows SEM images of the top view of the plane perpendicular to the aragonite *c*-axis for a sample fractured in uniaxial compression after air drying for 12 weeks. A jagged, tortuous crack path is observed

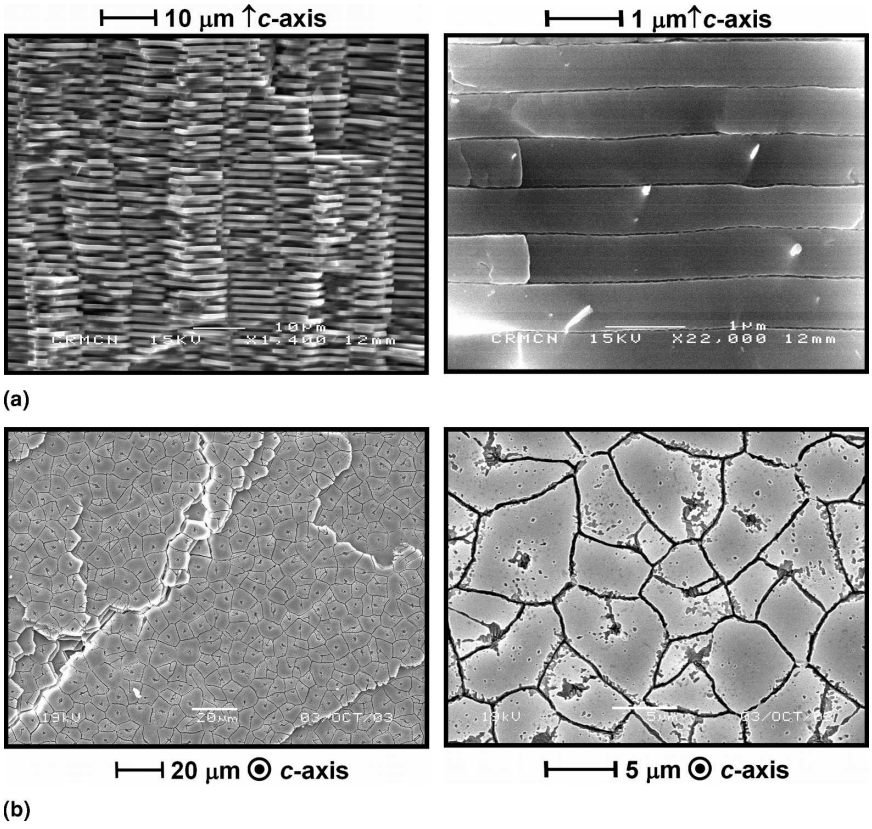


FIG. 4. SEM images of (a) side view of inner laminated, columnar nacreous microstructure of *Trochus niloticus* freshly fractured in 3-point bend and (b) top-down view of nacreous layer cleaved in uniaxial compression and dried in air for 3 months. ⊙ indicates the *c*-axis direction is out of (perpendicular to the plane of) the page.

that follows both within the individual tablets as well as along the tablet boundaries. Clear visualization of the tablet boundaries, center biomineralization nucleation sites, and fracture within individual tablets (presumably along the intratablet crystalline sector boundaries[10]), was observed, most likely due to macromolecular shrinkage. Image analysis yielded a maximum lateral tablet dimension (perpendicular to the aragonite *c*-axis) of 7.9 ± 1.7 μm and thickness (parallel to the aragonite *c*-axis) of 0.9 ± 0.2 μm (the ± symbol here and henceforth refers to one standard deviation). Figure 5 is a top-view (plane perpendicular to the aragonite *c*-axis) BSE image showing local heterogeneities in contrast, which emphasizes the intratablet sector structure and could be due to varying aragonite crystallographic orientation and/or mineral content between sectors.[50,51]

## 2. AFM

Figure 6(a) shows a top-view (plane perpendicular to the aragonite *c*-axis) CMAFM deflection image of the surface of an individual nacre layer produced by recent cleavage in uniaxial compression. The tablet boundaries are less distinguishable than those observed by SEM for the air-dried samples [Fig. 4(b)], most likely due to the more hydrated organic component keeping the tablets in closer contact. The surface of an individual tablet (plane perpendicular to the aragonite *c*-axis) is shown in the CM AFM deflection image of Fig. 6(b) [which is approximately the same length scale as the schematic shown in Fig. 1(c)] and possesses surface roughness due to topographical features ("nanoasperities") and a central nucleation site which is ~500 nm long and ~40 nm high. Figure 6(c) shows a CMAFM deflection image of the through thickness cross-section of an individual fractured nacre tablet corresponding to the central portion oriented at approximately 45° relative to the horizontal direction separated by two different planes of tablets with uniform nanoasperities. An interesting fracture morphology is observed with smaller cylindrical features through the thickness of the nacre tablet and an interior portion of the tablet containing interdigitated structures perpendicular to the long axis of the cylindrical elements. A higher resolution TMAFM plane amplitude image [Fig. 6(d), perpendicular to aragonite *c*-axis] enables direct visualization of the fine details of the nanoasperities on an individual nacre tablet, and corresponding height images yield values of 109.9 ± 37.4 nm in maximum lateral dimension perpendicular to the aragonite *c*-axis and 7.4 ± 3.2 nm in peak-to-valley height parallel to the aragonite *c*-axis. Each nanoasperity is observed to be composed of an assembly of smaller nanoasperities (previously referred to as nanograins[11]) 28.0 ± 11.9 nm in maximum lateral dimension. Figure 7 shows further magnified TMAFM amplitude images of the plane perpendicular to the aragonite *c*-axis, capturing the resolution of the individual smaller nanoasperities [approximately the same length scale as the schematic shown in Fig. 1(d)]. Here, organic fibrils are directly visualized on top of the nacre tablets and are measured to have a mean width of 8.8 ± 5.6 nm, end-to-end length of 52.1 ± 37.5 nm, and height of 0.96 ± 0.25 nm. The organic component appears to be primarily localized within the valleys of the nanoasperities. Figure 8 shows TMAFM phase images of regions similar to that shown in Fig. 7. Contrast in these images is sensitive to variations in surface properties such as friction, adhesion, (visco)elasticity, and composition. Figure 8 clearly demonstrates the presence of two different types of materials. Darker areas correspond to a greater cantilever lag and larger energy dissipation and hence support the previous identification (via height images) of the organic component (dark areas) and the nanoasperities (lighter areas). Figure 9 gives the probability histograms for all of the previous morphological features discussed measured using SEM and AFM, and Table I summarizes the means and standard deviations corresponding to these histograms.

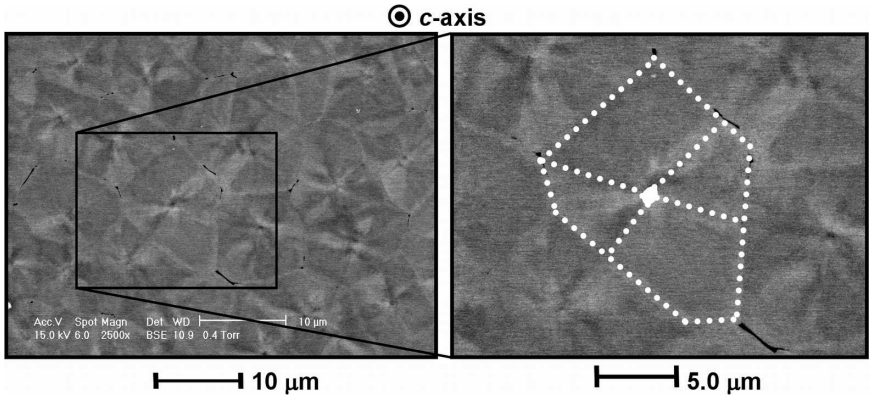


FIG. 5. Backscattered electron microscopy image of a top-down view of inner laminated, columnar nacreous microstructure of *Trochus niloticus* freshly cleaved in uniaxial compression, 50 μm scan (left) and a schematic of the outlines of an aragonite tablet on a magnified portion of this image (right). ⊙ indicates the *c*-axis direction is out of the page.

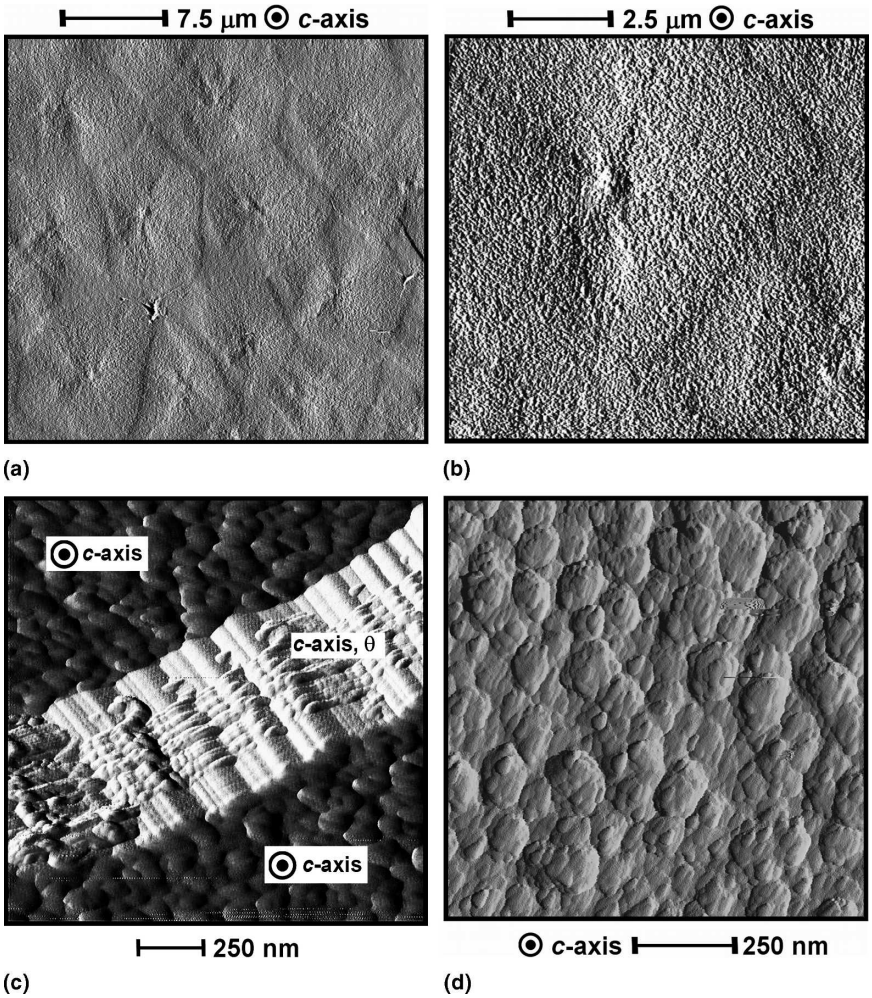


FIG. 6. (a, b, c) Contact mode deflection and (d) tapping mode amplitude atomic force microscopy (AFM) images of top down view of inner laminate columnar nacre of *Trochus niloticus* nacreous layer freshly cleaved in uniaxial compression; (a) 30 μm scan, (b) 10 μm scan, (c) 1.5 μm scan showing through-thickness fracture and microstructure of an individual nacre plate and (d) 1 μm scan. ⊙ indicates *c*-axis direction is out of the page.

## B. Nanoindentation

Figure 10(a) is a plot of multiple individual nanoindentation curves on loading and unloading (force versus depth) where each curve is on a different individual freshly cleaved *Trochus niloticus* nacre tablet (from the same sample). A maximum load of 1000 μN resulted in an indentation depth of ~65 nm. Some curves exhibited small "kinks" at a variety of different forces (typically in the hundreds of μN range) and depths while others were relatively smooth [Fig. 10(b)]. A marked and consistent change in slope was observed at ~73 μN force and ~7–15 nm depth [Fig. 10(c)], which is similar in value to the peak-to-valley height of the nanoasperities [Fig. 9(h)]. Plots of the averaged nanoindentation curves corresponding to different maximum loads are given in Fig. 11, comparing the freshly cleaved and artificial seawater soaked nacre. Increased hydration by soaking the nacre samples in artificial seawater resulted in an increase in depth of indentation for a given force (e.g., from ~68 to ~74 nm for a 1000 μN maximum force) and an increased residual displacement upon unloading (e.g., from ~23 to ~27 nm for a 1000 μN maximum force) for all maximum loads tested. Nacre samples soaked in artificial seawater also sometimes exhibited kinks in the individual nanoindentation curves (data not shown). All samples exhibited mechanical hysteresis.

## C. Nanoscale deformation

Figures 12(a)–12(c) are tapping mode AFM images (Q-scope) of the indented region of freshly cleaved nacre samples [individual tablets shown in the plane perpendicular to the aragonite *c*-axis; the length scale corresponds approximately to the schematic illustration shown in Fig. 1(c)], upon removal of maximum loads of 1000, 5000, and 10,000 μN, respectively, and Fig. 12(d) is for artificial seawater soaked nacre upon removal of a maximum load of 5000 μN. The features observed away from the indent region in all four images are the larger

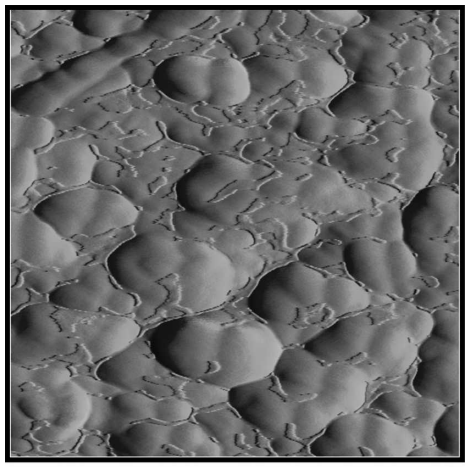


(a)

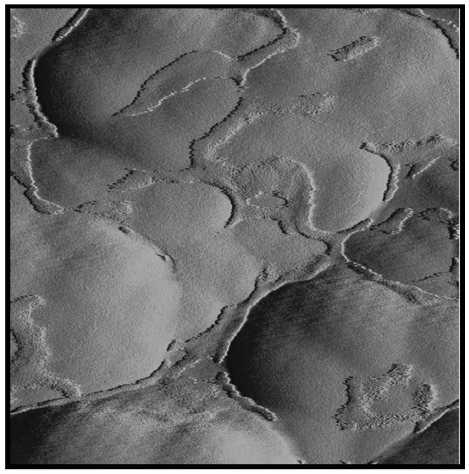


(b)

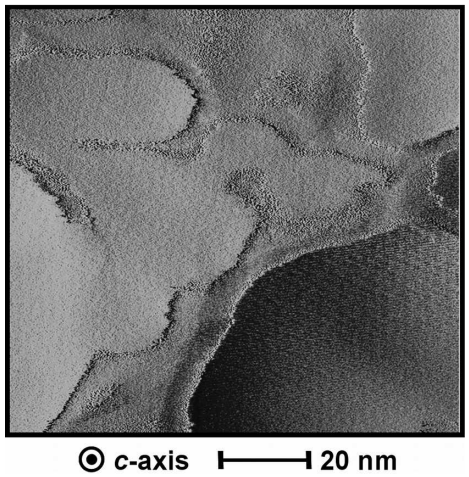


(c)

FIG. 7. Tapping mode amplitude atomic force microscopy images of nanoasperities and organic matrix on the top of an individual nacre tablet of *Trochus niloticus* that was freshly cleaved in uniaxial compression; (a) 500 nm scan, (b) 200 nm scan, and (c) 100 nm scan. ⊙ indicates *c*-axis direction is out of the page.

nanoasperity assemblies corresponding to those observed in Fig. 6(c). Residual deformation was clearly visible, exhibiting a central indent and a pileup zone indicating plastic flow of the material from beneath the indenter. No microcracks were evident within the residual indent region, in the pileup zone, or in the area immediately outside the residual indent. The nanoasperity assemblies were significantly flattened within the residual indent region. Figure 13 shows height profiles for indentations on freshly cleaved nacre showing pileup at maximum loads of 1000 and 5000 μN. For the 1000 μN maximum load, the average pileup height was ~21.1 ± 10.5 nm and spanned lateral distances from the edge of the indent of ~363 ± 49 nm (somewhat larger than that previously reported on *California red abalone*[11]).

### D. Estimation of material properties

#### 1. Work of indentation

The plastic work or mechanical hysteresis energy, $W_p$, was found to be 10.1 ± 1.8 mN nm for the freshly cleaved nacre and 9.2 ± 1.8 mN nm for the artificial seawater soaked nacre at a 1000 μN maximum load. The elastic work, $W_e$, yielded a value of 16.4 ± 1.0 mN nm for the freshly cleaved nacre and 16.0 ± 0.8 mN nm for the artificial seawater soaked nacre while the total work of deformation at a 1000 μN maximum load was 26.5 ± 1.6 mN nm and 25.2 ± 1.5 mN nm, respectively. All three mechanical works showed no statistically significant differences when comparing the two types of samples.

#### 2. O-P estimations of elastic moduli

For freshly cleaved nacre, average values of the elastic moduli ranged between 114 and 143 GPa, (depending on the maximum load) and for artificial seawater-soaked nacre, average values ranged between 101 and 126 GPa [Fig. 14(a)]. When the data for freshly cleaved nacre were compared with those of artificial seawater-soaked nacre at a given maximum load, all were found to be statistically different except for 250 and 500 μN maximum loads. For freshly cleaved nacre, elastic moduli compared at different loads were statistically different in 9/15 comparisons with 50–100, 100–250, 250–750, 500–750, 500–1000, and 750–1000 μN maximum loads being statistically similar. For artificial soaked nacre, elastic moduli compared at different loads were statistically different in 6/15 comparisons (50–250, 100–750, 100–1000, 250–500, 250–750, 250–1000 μN).

#### 3. O-P estimations of hardness

Average hardness values ranged between 9.7 and 11.4 GPa (depending on the maximum load) for the freshly cleaved nacre and 3.6 and 8.7 GPa for the artificial seawater soaked samples [Fig. 14(b)]. When comparing the data for freshly cleaved to artificial seawater

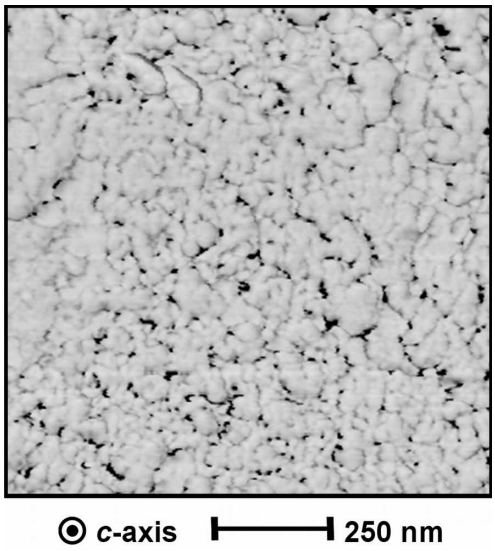


(a)

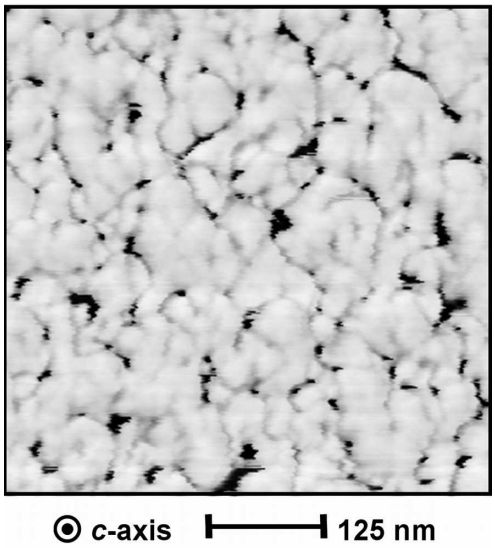


(b)

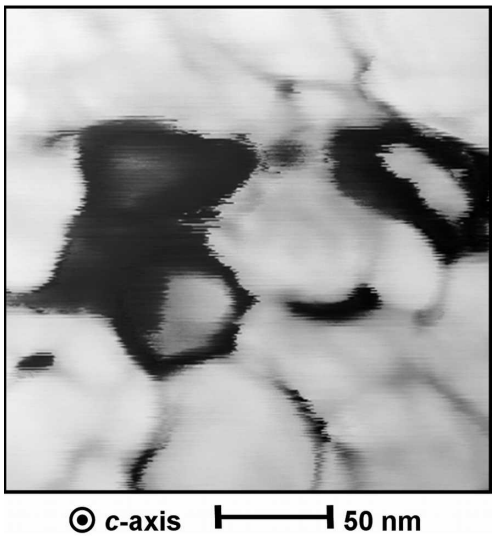


(c)

soaked nacre at a given maximum load, all were found to be statistically different. For freshly cleaved nacre almost no statistically significant differences were found as a function of maximum load (except for the 50–750 and 100–750 μN datasets). For artificial seawater-soaked nacre, hardnesses compared at different loads were statistically different in 6 of 15 comparisons where the 50 μN data compared to all the other loads were significantly different, as was the 500–1000 μN comparison.

### 4. O-P estimations of *H*/*E* ratio

*H*/*E* values [Fig. 14(c)] ranged between 0.072 and 0.096 (depending on the maximum load) for the freshly cleaved samples and between 0.034 and 0.084 for the artificial seawater soaked nacre. When the data for freshly cleaved nacre were compared to those of artificial seawater-soaked nacre at a given maximum load, all were found to be statistically different except for the 100 μN data. For the freshly cleaved samples, *H*/*E* values compared at different loads were statistically different in 10 of 15 comparisons (50–100, 50–250, 500–750, 500–1000, and 750–1000 μN were statistically similar). For the artificial seawater-soaked samples, *H*/*E* values compared at different loads were statistically different in 12 of 15 comparisons (100–250, 100–500, and 250–500 μN were statistically similar).

### 5. FEA

FEA simulations [Figs. 15(a) and 15(b)] were used to fit values for the elastic modulus and yield stress to nanoindentation data. Three experimental nanoindentation curves (1000 μN maximum load) were fit on both loading and unloading: the averaged curve [Figs. 15(c) and 15(d)], the highest curve, and the lowest curve for each of the two types of nacre samples. The elastic modulus of freshly cleaved nacre was found to be 92 ± 13 GPa (the standard deviation being due to the range in fits from low-to-average-to-high curves), whereas the nacre soaked in artificial seawater was found to have an elastic modulus of 79 ± 15 GPa [data plotted in Fig. 14(a) with the O-P estimations, a statistically insignificant differ comparing freshly cleaved and artificial seawater soaked due to the small number of data points, $n = 3$]. The yield strength of fresh nacre was found to be 11.1 ± 3.0 GPa, and that for nacre soaked in artificial seawater was found to be 9.0 ± 3.2 GPa (a statistically insignificant difference comparing freshly cleaved and artificial seawater

FIG. 8. Tapping mode phase atomic force microscopy images of nanoasperities and organic matrix on the top of an individual nacre tablet of *Trochus niloticus* that was freshly cleaved in uniaxial compression; (a) 1 μm scan, phase shift from −124° (darker) to +28° (lighter); (b) 500 nm scan, phase shift from −130° (darker) to +29° (lighter), and (c) 200 nm scan, phase shift from −105° (darker) to +64° (lighter). ⊙ indicates *c*-axis direction is out of the page.

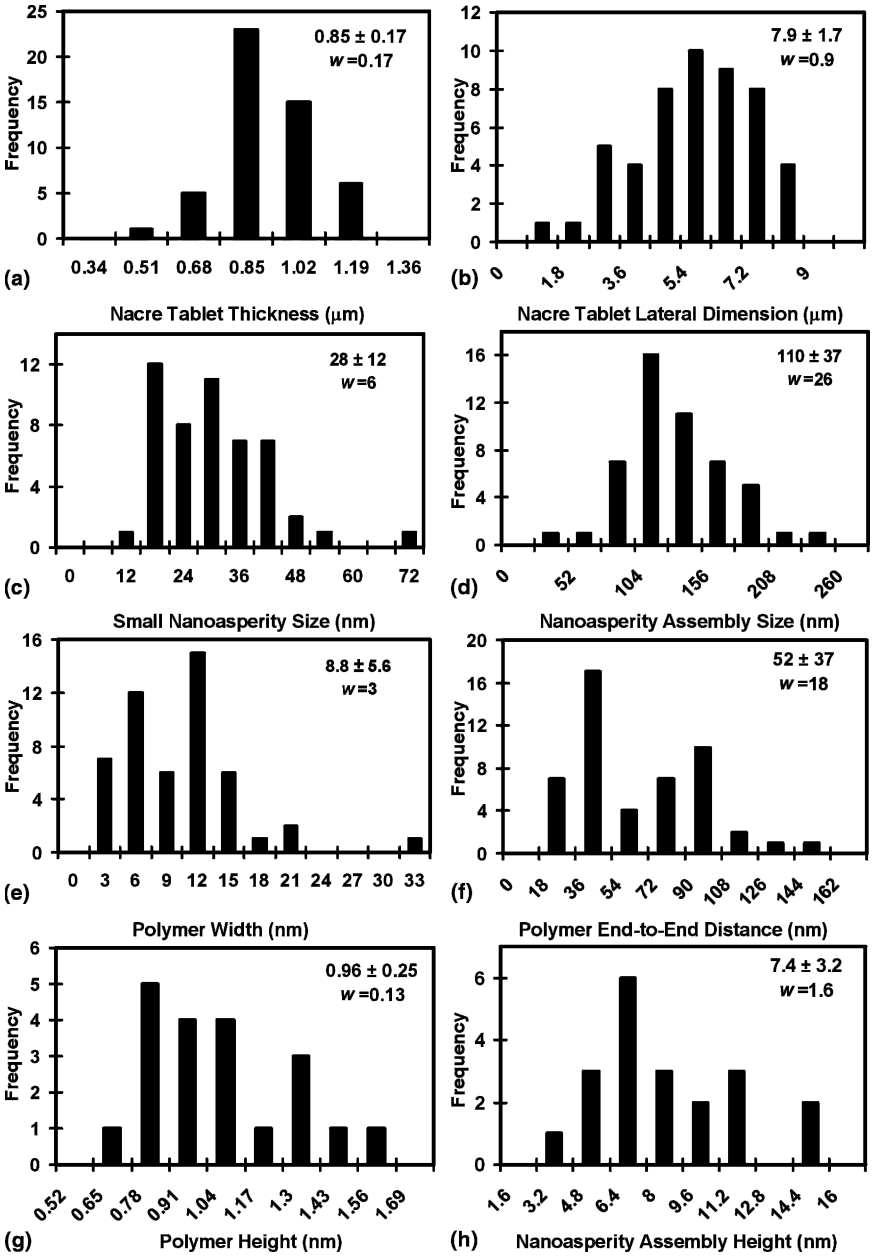


FIG. 9. Histograms of various features observed by (a,b) SEM and (c–h) AFM; the inset of numerical values indicates mean ± standard deviation for each dataset, *w* is the bin width (chosen based on Sturges' and Scott's rules[60,61]), and the number of datapoints for each histogram is >20.

TABLE I. Quantitative analysis of structural features *Trochus niloticus* nacre freshly cleaved in uniaxial compression, observed by SEM and AFM (number of datapoints measured for each feature $n > 20$).

| Technique | Feature | Mean ± standard deviation |
|---|---|---|
| SEM | nacre table thickness (// to *c* axis) | 0.9 ± 0.2 μm |
| SEM | nacre tablet maximum dimension (⊥ to *c* axis) | 7.9 ± 1.7 μm |
| TMAFM | maximum dimension of small nanoasperities (⊥ to *c* axis) | 28.0 ± 11.9 nm |
| TMAFM | maximum dimension of larger clusters of nanoasperities (⊥ to *c* axis) | 109.9 ± 37.4 nm |
| TMAFM | nanoasperity assembly height (// to *c* axis) | 7.4 ± 3.2 nm |
| TMAFM | polymer width (⊥ to *c* axis) | 8.8 ± 5.6 nm |
| TMAFM | polymer end-to-end length (⊥ to *c* axis) | 52.1 ± 37.5 nm |
| TMAFM | polymer height (// to *c* axis) | 0.96 ± 0.25 nm |

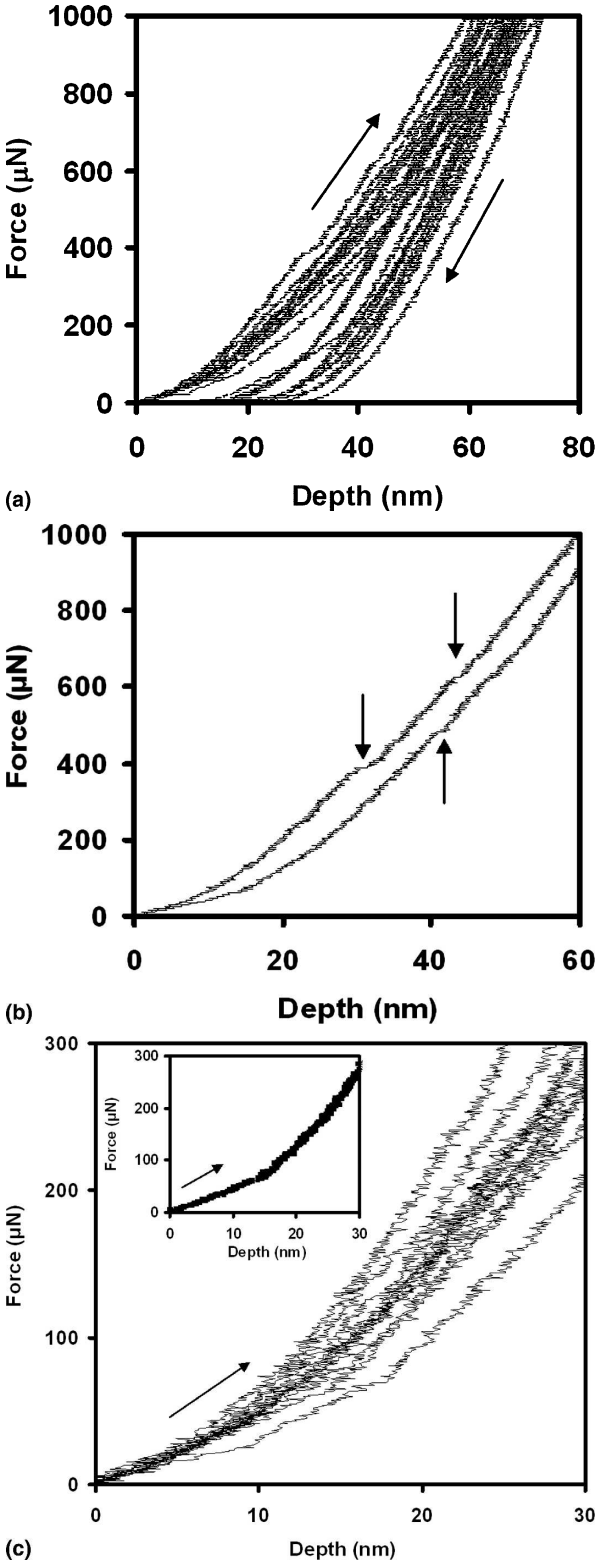


FIG. 10. Individual nanoindentation curves each on a single freshly cleaved *Trochus niloticus* nacre tablet (a) multiple curves on loading and unloading up to a maximum load of 1000 μN, (b) two of the curves from the dataset shown in (a) on loading with arrows indicating minor inflections, and (c) multiple curves on loading and unloading up to a maximum load of 300 μN; inset is one individual curve from this dataset with a pronounced variation in slope at ~15 nm and ~73 μN.

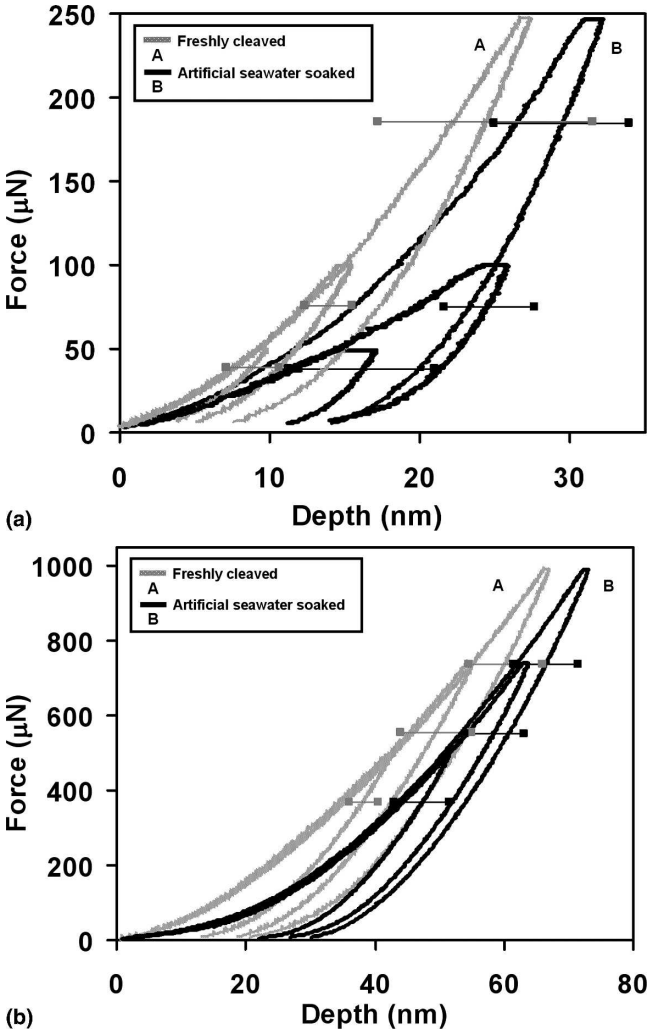


FIG. 11. Average nanoindentation curves on freshly cleaved and artificial seawater-soaked individual *Trochus niloticus* nacre tablets on loading and unloading as a function of maximum load; (a) 50, 100, and 250 μN maximum loads and (b) 500, 750, and 1000 μN maximum loads. The horizontal error bars represent the standard deviation for that particular dataset.

soaked due to the small number of curves fit, $n = 3$). Figure 16(a) shows a contour of the maximum principal stress on the surface when indented to 1000 μN, revealing very large tensile stresses in the pileup region. Figure 16(b) shows the corresponding contour after unloading, also revealing very high tensile principal stresses in the pileup region (a characteristic stress state seen in the extruded pileup region of indented materials). Note that cracks were not observed in the experiments, indicating an ability to withstand these high tensile stresses at small length scales. Figures 16(c) and 16(d) show two-dimensional height maps at the point of maximum load (1000 μN) before and after unloading, respectively. Figure 16(d) reveals the residual indent as well as the surrounding pileup resulting in plastic extrusion from under the probe tip. A one-dimensional height profile

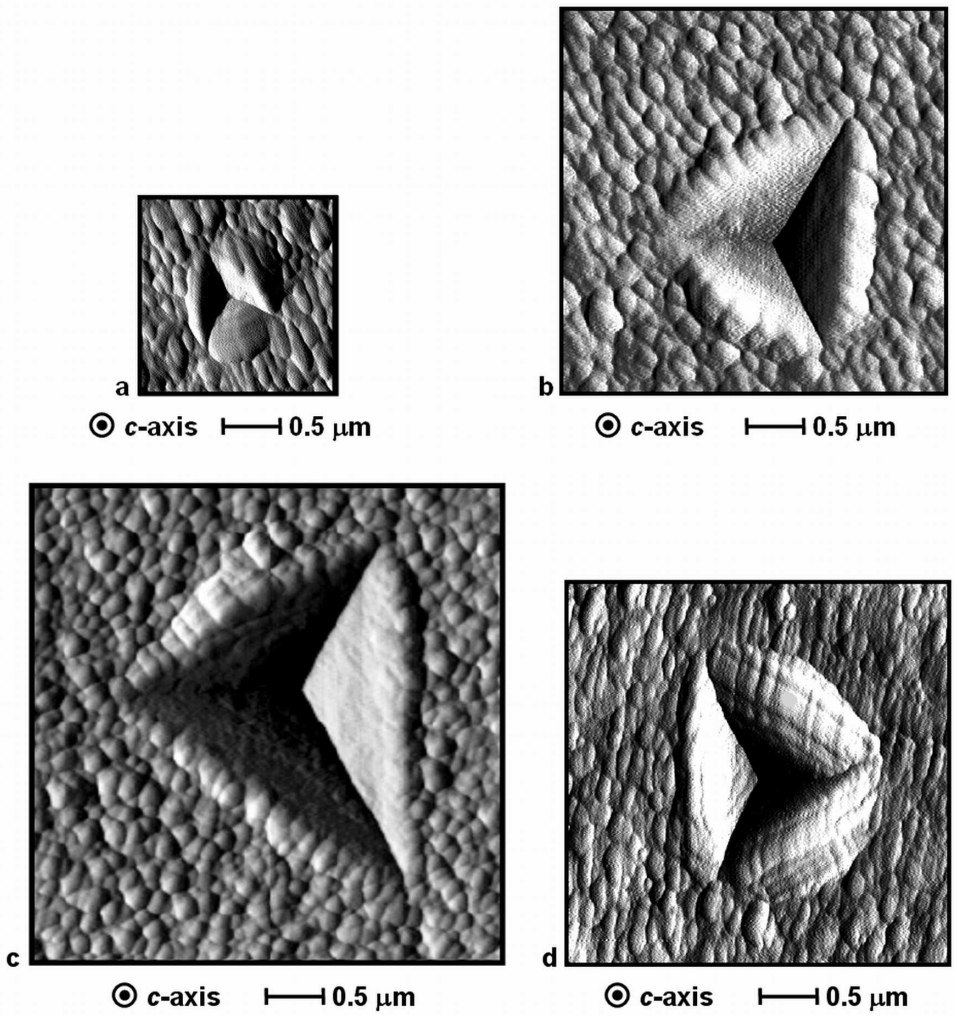


FIG. 12. Tapping mode AFM images of top down view of residual nanoindentation impression on individual freshly cleaved *Trochus niloticus* nacre tablet; (a) maximum load = 1000 μN and 1.8 μm scan, (b) maximum load = 5000 μN and 3 μm scan, (c) maximum load = $1 \times 10^4$ μN and 3.7 μm scan, and (d) nacre incubated in artificial seawater for 10 weeks and maximum load = 5000 μN, 3.0 μm scan. ⊙ indicates *c*-axis direction is out of the page.

corresponding to the same radial directions as shown in the inset of Fig. 13 is plotted in Fig. 13 along with the experimental profiles.

## IV. DISCUSSION

### A. Ultrastructure

High-resolution AFM images of surface morphology elucidate new details of the complex hierarchical structure at length scales below that of an individual nacre tablet including nanoscale resolution of the tablet cross-section, the dimensions, location, and conformation of the organic matrix, individual and assemblies of nanoasperities. Identification the organic component (versus mineral-based nanoasperities) was made by a comparison of topographic and phase images; topographic images showed a typical tortuous appearance characteristic of macromolecules at surface[45] and phase images showed that these regions had greater energy dissipative character. Overall, the AFM results are consistent with suggestions of an intratablet sector structure,[10] nanometer-sized asperities comprising larger assemblies within individual nacre tablets,[11] and the presence of smaller cylindrical crystalline elements.[17] The mean nanoasperity size reported here for the nacre of *Trochus niloticus* (28 ± 12 nm) is similar to that reported for California red abalone nacre (~32 nm).[11] AFM imaging of the organic matrix yields low heights of ~1 nm, which corresponds approximately to the thickness of an individual polymer chain and an irregular conformation, most likely due to collapse and denaturation during dehydration and/or partial removal during cleavage leaving only the most strongly bound macromolecules, presumably the polyanionic layer in closest proximity to the mineral tablets.[24]

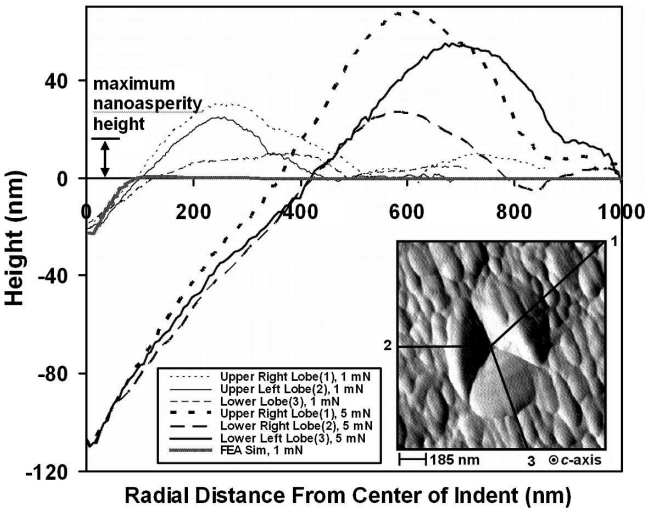


FIG. 13. Height profiles for 1000 and 5000 μN maximum load residual indents taken from tapping mode AFM images on freshly cleaved individual *Trochus niloticus* nacre tablets. The inset is an AFM image of the residual indent for the 1000 μN maximum load. [Corresponding to the image given in Fig. 12(a)].

The spatial conformation and heterogeneities observed in the organic component are also likely to be highly dependent on the sample preparation procedures. No features were clearly identified as mineral bridges, which could have been due to the fact that the smaller scan size images [Figs. 6(c), 6(d), and 7] probe only smaller surface areas and the larger scan size images [Figs. 6(a) and 6(b)] may be unable to resolve the difference between nanoasperities and mineral bridges. Another study[20] on samples of *Haliotis laevigata* nacre that was cleaved, abrasively ground, processed with acryl polishing paste, and partially demineralized with 0.5M ethylene diamine-tetra-acetic acid (EDTA) showed, via CMAFM imaging in fluid, larger filaments ~50 nm in diameter localized around the borders of the individual tablets and identified them as collagen fibers; no such features were observed in this study.

## B. Nanoindentation

The consistent change in slope observed in the nanoindentation curves for freshly cleaved *Trochus niloticus* nacre at ~73 μN force and ~7–15 nm depth [Fig. 9(c)] is similar to a phenomenon previously reported for thermally etched California red abalone nacre, which takes place at ~25 μN and ~30 nm depth and has been suggested to be caused by a change in mechanism from plastic deformation and flattening of nanoasperities to deformation of the tablet over larger length scales.[42] The distance range over which the slope change was observed to take place in these experiments on *Trochus niloticus* correlates well with the measured height of the nanoasperity assemblies [Fig. 9(h)] and lends credence to this

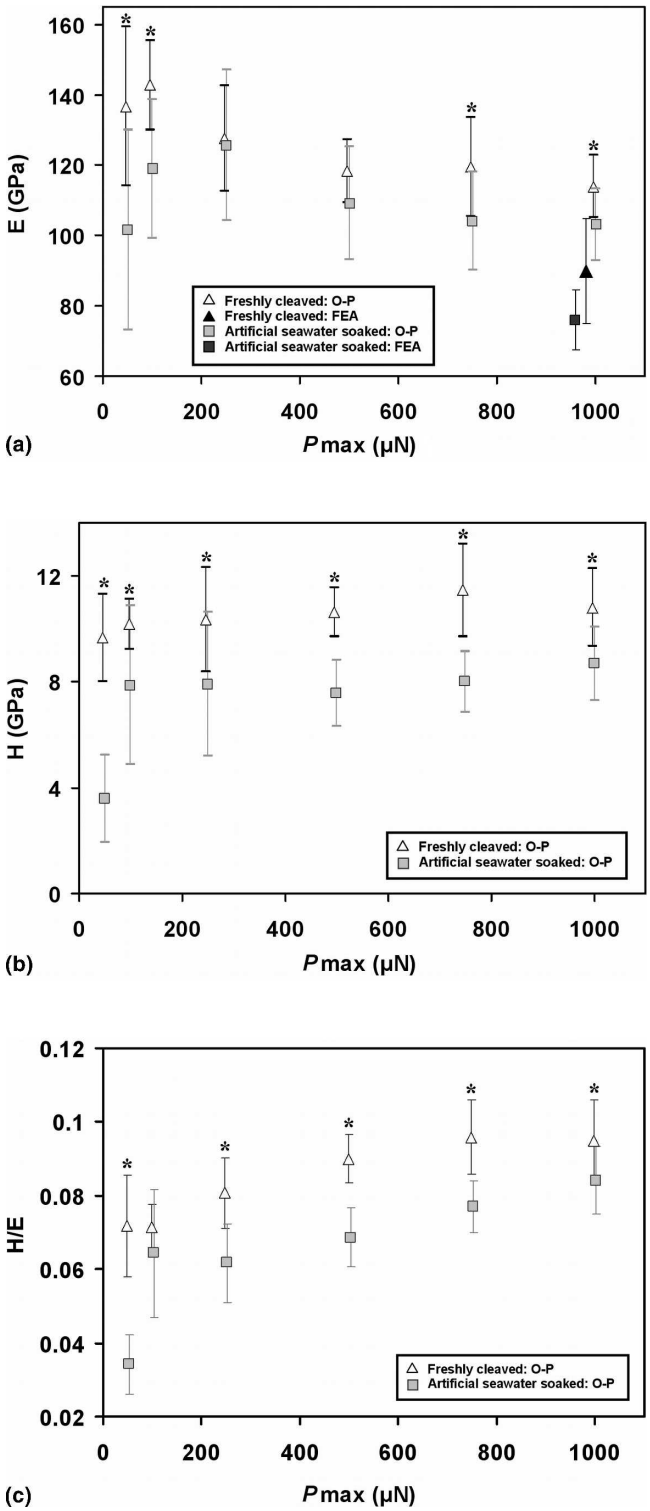


FIG. 14. Mechanical properties derived from nanoindentation curves on freshly cleaved and artificial seawater-soaked individual *Trochus niloticus* nacre tablets as a function of maximum load; (a) average elastic moduli *E*, using both Oliver–Pharr analysis and FEA simulations, (b) average hardness *H* derived using the Oliver–Pharr analysis, and (c) *H*/*E* plot. The vertical error bars represent the standard deviation for that particular dataset and the data sets marked with an asterisk (*) indicate statistically significant differences ($p < 0.05$) between the freshly cleaved and artificial seawater-soaked samples.

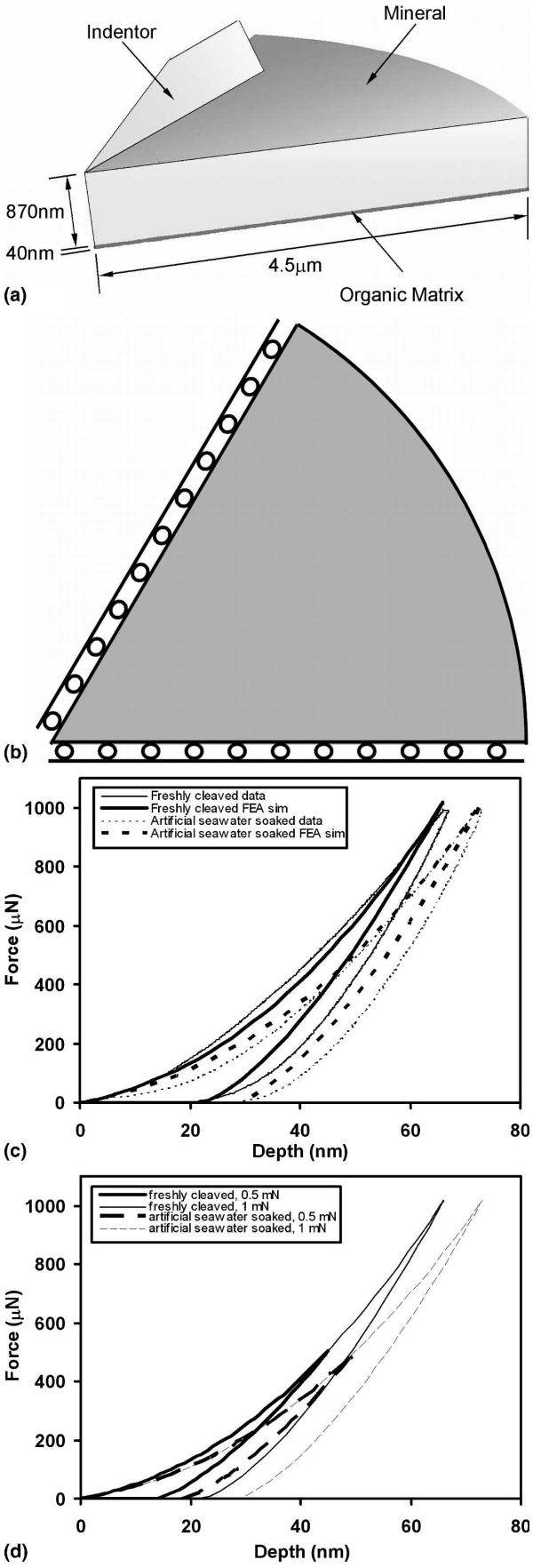


idea. Small kinks observed in the individual curves may be due to interfacial collapse,[42] which is seen to take place over a small distance range of a few nanometers. Table II summarizes all of the various nanomechanical properties measured in this study comparing the freshly cleaved and artificial seawater soaked nacre samples at a maximum load of 1000 μN.

### C. Elastic moduli

The elastic moduli obtained at a 1000 μN maximum load by the O-P method (114 ± 9 GPa and 103 ± 10 GPa for the freshly cleaved and artificial seawater soaked samples, respectively) were 21–26% higher than those estimated by the FEA simulations (92 ± 13 GPa and 79 ± 15 GPa for the freshly cleaved and artificial seawater soaked samples, respectively), which is a statistically significant difference. The accuracy of the O-P predictions depends on the estimation of the contact area function, and for the case of pileup (as observed via AFM), the O-P method underestimates this value, thus overestimating the moduli (since $E \sim 1/\sqrt{A}$). The FEA simulations more specifically account for the geometric details of the Berkovich geometry and also capture the details of the entire elastic–plastic loading/unloading process. Hence, FEA is expected to provide a more accurate estimation of the moduli. However, the results indicate that a rather good approximation is obtained with the O-P fits. The FEA simulations predict the residual depth of the indent well but underestimate the experimentally observed pileup height (Fig. 13), most likely because it does not account for deformation of the nanoasperities.

Overall, values obtained from nanoindentation experiments were consistent with macroscopic measurements of aragonite.[35] The O-P moduli values for the nacre of *Trochus niloticus* were found to be somewhat higher than that reported for diamond-cut, mechanically ground, polished, and hydrated nacre from California red abalone (60–80 GPa) at similar maximum loads (800 μN) calculated using the O-P method,[11] which could be due to variations in sample preparation, species, age, *c*-axis orientation, location within in the shell, and/or degree of hydration. A decrease in modulus with increasing maximum load (−17% from 50 to 1000 μN) was observed, suggesting a length scale dependence. Hydration was found to generally result in a decrease in the moduli

FIG. 15. Isotropic elastic–plastic FEA nanoindentation simulations; (a) schematic of model, (b) boundary conditions to ensure one sixth symmetry (top view), (c) simulations fit to average nanoindentation data on loading and unloading for 1000 μN maximum load. Input parameters were as follows: freshly cleaved nacre ($E$ = 90 GPa, $\sigma_Y$ = 11GPa) and artificial seawater-soaked nacre ($E$ = 76 GPa, $\sigma_Y$ = 8.4 GPa), and (d) simulations for both nacre samples for maximum loads of 500 and 1000 μN.

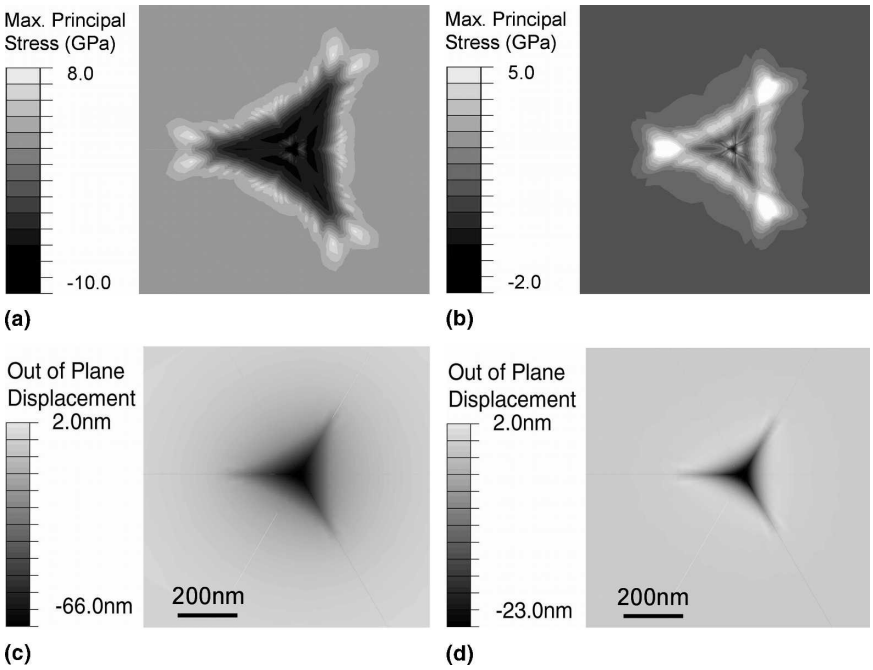


FIG. 16. The top view (plane perpendicular to nacre tablet *c*-axis) of the contour for the maximum principal stress (a) at a maximum load of 1000 μN, and (b) after unloading from 1000 μN and height contours, (c) at a maximum load of 1000 μN, and (d) after unloading from 1000 μN. Since only one sixth of the material is modeled, the plot here consists of six identical images from numerical simulations (E = 90 GPa, $\sigma_Y$ = 11 GPa).

(−1.5% to −26%). However, the elastic work for the freshly cleaved and seawater soaked nacre was found to be statistically similar; this result was due to the fact the unloading slopes were similar, but the maximal depths were different (they varied only by ~6 nm), resulted in a statistically different contact areas calculated by the O-P method, and thus yielded statistically different values of moduli. This suggests that small variations in the surface nanoasperity structure can result in calculations of statistically different values of moduli not reflective of bulk tablet nanomechanical properties.

### D. O-P Hardness and *H*/*E*

Hydration was observed to conclusively decrease the O-P hardness (−20% to −63%). Once again, this is not consistent with the statistically similar differences in plastic or total work due to the statistically different contact areas calculated by the O-P method. The hardness of the freshly cleaved samples was found to have minimal dependence on maximum load and the seawater-soaked samples had a slight increase with maximum load. Due to pileup, an underestimation in contact area is expected to

TABLE II. Nanoindentation properties (at a maximum load of 1000 μN) of nacre from *Trochus niloticus* comparing freshly cleaved samples to hydrated samples incubated in artificial seawater for 10 weeks. Reported values are means ± one standard deviation.

| Property | *n* | Fresh | Hydrated | $p < 0.05$ |
|---|---|---|---|---|
| Maximal depth, $h_{max}$ (nm) | 14 | 67.0 ± 3.2 | 72.9 ± 4.6 | Yes |
| O-P maximal contact area $A_c$ ($\mu m^2$) | 14 | 0.093 ± 0.012 | 0.117 ± 0.019 | Yes |
| Residual depth, $h_p$ (nm) | 14 | 20.8 ± 3.6 | 30.1 ± 5.3 | Yes |
| Plastic work, $W_p$ (mN nm) | 14 | 10.1 ± 1.8 | 9.2 ± 1.8 | No |
| Elastic work, $W_c$ (mN nm) | 14 | 16.4 ± 1.0 | 16.0 ± 0.8 | No |
| Total work, $W_T$ (mN nm) | 14 | 26.5 ± 1.6 | 25.2 ± 1.5 | No |
| O-P modulus, *E* (GPa) | 14 | 114.0 ± 8.8 | 103.0 ± 10.1 | Yes |
| O-P hardness, *H* (GPa) | 14 | 10.8 ± 1.5 | 8.7 ± 1.4 | Yes |
| O-P (*H*/*E*) | 14 | 0.095 ± 0.011 | 0.084 ± 0.009 | Yes |
| FEA modulus, *E* (GPa) | 3 | 92 ± 13 | 79 ± 15 | No |
| FEA yield stress, $\sigma_Y$ (GPa) | 3 | 11.1 ± 3.0 | 9.0 ± 3.2 | No |
| Pileup height (AFM, nm) | 3 | 21.1 ± 10.5 | ... | ... |
| Lateral pileup distance[a] (AFM, nm) | 3 | 363.9 ± 49.3 | ... | ... |
| Residual indent area excluding pileup (AFM, $\mu m^2$) | 3 | 0.072 | ... | ... |

[a]Measured from outer edge of indent to outer edge of pileup area.

lead to an overestimation in the absolute values of hardness ($H \sim 1/A$).

### E. Nanoscale deformation

AFM inspection showed the existence of nanoasperity flattening within the residual indent region, plastic deformation, and no microcracks in the pileup region (as might be expected in a larger scale indentation process). This suggests that the length scale of the material and the indent process reveals a ductility not expected to be present at larger length scales (where a ceramic would be expected to exhibit microcracking under the tensile stresses observed in the pileup region and fail in a brittle manner). The observed ductility may be due to the small length scale, ruling out defect initiated microcracking (i.e., the Griffith flaw argument) and/or may indicate that occluded biomacromolecules within the tablet further mitigate any defects and add ductility to the deformation process. The configuration of the pileup zones on the border of the indents (Figs. 12, 13) demonstrates that the nanoasperities have the ability to undergo plastic deformation to accommodate the strain imposed by the indenter tip. Imaging of the indents (Fig. 12) is consistent with these results, as the region indented in hydrated nacre exhibits a much greater plastic deformation than the one in fresh nacre for the same load, consistent with the fact that the hydrated nacre tablet indicates a lower yield stress than those of the fresh nacre tablets.

### F. Relation of nacre tablet deformation to larger scale deformation mechanisms

It has been suggested that the nacre tablets serve as the primary load-bearing elements where the load is transferred through the bridging organic matrix via a shear lag mechanism.[5,40,52] The unique combination of both high local stiffness and strength of the individual nacre tablets observed here support this argument and likely facilitate energy dissipating mechanisms such as intertablet shear and pullout (which are experimentally observed[1]) rather than brittle intratablet failure. While intratablet fracture was observed in Fig. 4(d), this was after lengthy air drying, in particular of the intratablet organic matrix, likely leading to a reduction in tablet strength. Intertablet shear and pullout also allow for additional energy dissipation via extension and progressive unfolding of protein modules in the organic matrix (i.e., rupture of "sacrificial" weaker bonds).[40,41,53] It has also been suggested that interacting nanoasperities and mechanical interlocking provide resistance to interfacial sliding, thus determining the level of stress needed to initiate inelastic strain.[3,37] The existence of a finer nanoasperity structure arranged into assemblies of larger nanoasperities would provide additional lateral resistance at an even smaller length scales than previously thought. At high enough stress values, our data suggests that plastic deformation of the nanoasperities can take place initially and may act as a "safety mechanism," prior to intertablet shear.

## ACKNOWLEDGMENTS

This research was supported by the United States Army through the Massachusetts Institute of Technology (MIT) Institute for Soldier Nanotechnologies, under Contract No. DAAD-19-02-D0002 with the Unites States Army Research Office. The content does not necessarily reflect the position of the government, and no official endorsement should be inferred. The authors would like to thank the MIT Undergraduate Research Opportunity Program, the Center for Materials Science and Engineering at MIT, Alan Schwartzman and the MIT Department of Materials Science and Engineering, Nanomechanical Technology Laboratory, and Alain Baronnet and the Centre de Recherche de la Matière Condensée et des Nanosciences, Université de Marseille-Luminy, France.

## REFERENCES

1. A.P. Jackson, J.F.V. Vincent, and R.M. Turner: The mechanical design of nacre. *Proc. R. Soc. London B Biol. Sci.* **234,** 415 (1988).
2. S. Weiner and L. Addadi: Design strategies in mineralized biological materials. *J. Mater. Chem.* **7,** 689 (1997).
3. R.Z. Wang, Z. Suo, A.G. Evans, N. Yao, and I.A. Aksay: Deformation mechanisms in nacre. *J. Mater. Res.* **16,** 2485 (2001).
4. R. Menig, M.H. Meyers, M.A. Meyers, and K.S. Vecchio: Quasi-static and dynamic mechanical response of *Haliotis rufescens* (abalone) shells. *Acta Mater.* **48,** 2383 (2000).
5. A.P. Jackson, J.F.V. Vincent, and R.M. Turner: Comparison of nacre with other ceramic composites. *J. Mater. Sci.,* **25,** 3173 (1990).
6. J.D. Currey: Mechanical properties of mother of pearl in tension. *Proc. R. Soc. London B Biol. Sci.* **196**(1125), 443 (1977).
7. H.K. Erban: On the structure and growth of the nacreous tablets in gastropods. *Biomineralisation* **7,** 14 (1974).
8. J.D. Taylor, W.J. Kennedy, and A. Hall: Shell structure and mineralogy of the bivalvia: Introduction *Nuculacea-Trigonacea. Bull. Brit. Museum Natural. History Zool.* (Suppl. 3): 1 (1969).
9. D.J.M. Bevan, E. Rossmanith, D.K. Mylrea, S.E. Ness, M.R. Taylor, and C. Cuff: On the structure of aragonite—Lawrence Bragg revisited. *Acta Crystallogr. B. Struct. Sci. B* **58,** 448 (2002).
10. H. Mutvei: Ultrastructural characteristics of the nacre in some gastropods. *Zool. Scr.* **7,** 287 (1978).
11. X. Li, W-C. Chang, Y.J. Chao, R. Wang, and M. Chang: Nanoscale structural and mechanical characterization of a natural nanocomposite material: The shell of red abalone. *Nano Lett.* **4,** 613 (2004).
12. G. Bevelander and H. Nakahara: An electron microscope study of the formation of the nacreous layer in the shell of certain bivalve molluscs. *Calc. Tiss. Res.* **3,** 84 (1969).
13. K. Wada: Nucleation and growth of aragonite crystals in the nacre of some bivalve molluscs. *Biomineralisation* **6,** 141 (1972).
14. H. Mutvei: On the internal structures of the nacreous tablets in molluscan shells. *Scanning Electron Microsc.* **2,** 457 (1979).
15. T.E. Schäffer, C. Ionescu-Zanetti, R. Proksch, M. Fritz, D.A. Walters, N. Almqvist, C.M. Zaremba, A.M. Belcher,

B.L. Smith, G.D. Stucky, D.E. Morse, and P.K. Hansma: Does abalone nacre form by heteroepitaxial nucleation or by growth through mineral bridges? *Chem. Mater.* **9,** 1731 (1997).
16. S. Manne, C.M. Zaremba, R. Giles, L. Huggins, D.A. Walters, A. Belcher, D.E. Morse, G.D. Stucky, J.M. Didymus, S. Mann, and P.K. Hansma: Atomic force microscopy of the nacreous layer in mollusc shells. *Proc. R. Soc. London B Bio. Sci.* **256,** 17 (1994).
17. H. Mutvei: Ultrastructural studies on cephalopod shells, Part 1: The septa and siphonal tube in *Nautilus. Bull. Geol. Inst. Univer. Upsala* (N.S.) **3,** 237 (1972).
18. X. Shen, A.M. Belcher, P.K. Hansma, G.D. Stucky, and D.E. Morse: Molecular cloning and characterization of lustrin A, a matrix protein from shell and pearl nacre of *Haliotis rufescens. J. Bio. Chem.* **272,** 32472 (1997).
19. Y. Zhang, L. Xie, Q. Meng, T. Jiang, R. Pu, L. Chen, and R. Zhang: A novel matrix protein participating in the nacre framework formation of pearl oyster, *Pinctada fucata. Comp. Biochem. Physiol. Part B* **135,** 565 (2003).
20. S. Blank, M. Arnold, S. Khoshnavaz, L. Treccani, M. Kuntz, K. Mann, G. Grathwohl, and M. Fritz: The nacre protein perlucin nucleates growth of calcium carbonate crystals. *J. Microsc.* **212,** 280 (2003).
21. F. Song, A.K. Soh, and Y.L. Bai: Structural and mechanical properties of the organic matrix layers of nacre. *Biomaterials* **24,** 3623 (2003).
22. F. Song, X.H. Zhang, and Y.L. Bai: Microstructure and characteristics in the organic matrix layers of nacre. *J. Mater. Res.* **17,** 1567 (2002).
23. B.A. Wustman, D.E. Morse, and J.S. Evans: Structural analyses of polyelectrolyte sequence domains within the adhesive elastomeric biomineralization protein lustrin A. *Langmuir* **18,** 9901 (2002).
24. S. Weiner and W. Traub: Macromolecules in mollusc shells and their functions in biomineralization. *Philos. Trans. R. Soc. London, Series B Bio. Sci.* **304,** 425 (1984).
25. I.M. Weiss, S. Kaufmann, K. Mann, and M. Fritz: Purification and characterization of perlucin and perlustrin, two new proteins from the shell of the mollusc *Haliotis laevigata. Biochem. Biophys. Res. Commun.* **267,** 17 (2000).
26. I.M. Weiss, C. Renner, M.G. Strigl, and M. Fritz: A simple and reliable method for the determination and localization of chitin in abalone nacre. *Chem. Mater.* **14,** 3252 (2002).
27. L. Pereira-Mouriès, M. Almeida, C. Ribeiro, J. Peduzzi, M-J. Barthélemy, C. Milet, and E. Lopez: Soluble silk-like organic matrix in the nacreous layer of the bivalve *Pinctada maxima. Eur. J. Biochem.* **269,** 4994 (2002).
28. L. Bédouet, M.J. Schuller, F. Marin, C. Milet, E. Lopez, and M. Giraud: Soluble proteins of the nacre of the giant oyster *Pinctada maxima* and of the abalone *Haliotis tuberculata:* Extraction and partial analysis of nacre proteins. *Comp. Biochem. Physiol. Part B: Biochem. Mol. Bio.* **128,** 389 (2001).
29. C.E. Bowen and H. Tang: Conchiolin-protein in aragonite shells of mollusks. *Comp. Biochem. Physiol. Part A: Phys.* **115A,** 269 (1996).
30. S. Weiner and W. Traub: X-ray diffraction study of the insoluble organic matrix of mollusk shells. *FEBS Lett.* **111,** 311 (1980).
31. S. Weiner, Y. Talmon, and W. Traub: Electron diffraction of mollusc shell organic matrices and their relationship to the mineral phase. *Int. J. Biol. Macromol.* **5,** 325 (1983).
32. N. Watabe: Studies on shell formation XI. Crystal-matrix relationships in the inner layers of mollusk shells. *J. Ultrastruct. Res.* **12,** 351 (1965).
33. A.M. Belcher, X.H. Wu, R.J. Christensen, P.K. Hansma, G.D. Stucky, and D.E. Morse: Control of crystal phase switching and orientation by soluble mollusc-shell proteins. *Nature* **381,** 56 (1996).
34. R.Z. Wang, H.B. Wen, F.Z. Cui, H.B. Zhang, and H.D. Li: Observations of damage morphologies in nacre during deformation and fracture. *J. Mater. Sci.* **30,** 2299 (1995).
35. *Handbook of Elastic Properties of Solids, Liquids and Gases,* edited by M. Levy, H. Bass, R. Stern, A.G. Every, and W. Sachse (Academic, San Diego, CA, 2001).
36. J.D. Currey and J.D. Taylor: The mechanical behavior of some molluscan hard tissues. *J. Zool. London* **173,** 395 (1974).
37. A.G. Evans, Z. Suo, R.Z. Wang, I.A. Aksay, M.Y. He, and J.W. Hutchinson: Model for the robust mechanical behavior of nacre. *J. Mater. Res.* **16,** 2475 (2001).
38. D.R. Katti, S.M. Pradhan, and K.S. Katti: Modeling the organic-inorganic interfacial nanoasperities in a model bio-nanocomposite, nacre. *Rev. Adv. Mater. Sci.* **6,** 162 (2004).
39. B. Ji and H. Gao: A study of fracture mechanisms in biological nano-composites via the virtual internal bond model. *Mater. Sci. Eng. A* **366,** 96 (2004).
40. H.J. Qi, B.J.F. Bruet, J.S. Palmer, C. Ortiz, and M.C. Boyce: Micromechanics and macromechanics of the tensile deformation of nacre, in *Mechanics of Biological Tissues,* Proceedings of International Union of Theoretical and Applied Mechanics (IUTAM), edited by G.A. Holzapfel and R.W. Ogden (Springer Verlag, Graz, Austria, 2005), p. 175.
41. H.J. Qi, C. Ortiz, and M.C. Boyce: Protein forced unfolding and its effects on the finite deformation stress-strain behavior of biomacromolecular solids, in *Structure and Mechanical Behavior of Biological Materials,* edited by P. Fratzl, W.J. Landis, R. Wang, and F.H. Silver (Mater. Res. Soc. Symp. Proc., **874,** Warrendale, PA, 2005), L4.31.
42. F. Barthelat and H.D. Espinosa: Elastic properties of nacre aragonite tablets, presented at the SEM Annual Conference and Exposition on Experimental and Applied Mechanics, Session 68, Paper 187, Charlotte, North Carolina, 2003; and F. Barthelat and H.D. Espinosa: Mechanical properties of nacre constituents: An inverse method approach, in *Mechanical Properties of Bioinspired and Biological Materials,* edited by C. Viney, K. Katti, F-J. Ulm, and C. Hellmich (Mater. Res. Soc. Symp. Proc. **844,** Warrendale, PA, 2005), Y.7.5.1, p. 67.
43. M.T. Hanson: The elastic field for spherical hertzian contact including sliding friction for transverse isotropy. *J. Tribology* **114,** 606 (1992).
44. W.C. Oliver and G.M. Pharr: An improved technique for determining hardness and elastic modulus using load and displacement sensing indentation experiments. *J. Mater. Res.* **7,** 1564 (1992).
45. S.S. Sheiko and M. Moller: Visualization of macromolecules: A first step to manipulation and controlled response. *Chem. Rev.* **101,** 4099 (2001).
46. D.C. Harris: *Quantitative Chemical Analysis,* 4th ed. (W. H. Freeman and Company, New York, 1995.).
47. E.M. Arruda and M.C. Boyce: A three-dimensional constitutive model for the large stretch behavior of rubber-elastic materials. *J. Mech. Phys. Solids* **41,** 389 (1993).
48. J.E. Bischoff, E.M. Arruda, and K. Grosh: Orthotropic hyperelasticity in terms of an arbitrary molecular chain model. *J. Appl. Mech.* **69,** 198 (2002).
49. J.E. Bischoff, E.M. Arruda, and K. Grosh: A microstructurally based orthotropic hyperelastic constitutive law. *J. Appl. Mech.* **69,** 570 (2002).
50. J.G. Skedros, R.D. Bloebaum, K.N. Bachus, and T.M. Boyce: The meaning of graylevels in backscattered electron images of bone. *J. Biomed. Mater. Res.* **27,** 47 (1993).
51. G.E. Lloyd: Atomic number and crystallographic contrast images with the SEM: A review of backscattered electron techniques. *Min. Mag.* **51,** 3 (1987).

52. S.P. Kotha, Y. Li, and N. Guzelsu: Micromechanical model of nacre tested in tension. *J. Mater. Sci.* **36,** 2001 (2001).
53. B.L. Smith, T.E. Schäffer, M. Viani, J.B. Thompson, N.A. Frederick, J. Kindt, A. Belcher, G.D. Stucky, D.E. Morse, and P.K. Hansma: Molecular mechanistic origin of the toughness of natural adhesives, fibres and composites. *Nature* **399,** 761 (1999).
54. C.G. Kontoyannis and N.V. Vagenas: Calcium carbonate phase analysis using XRD and FT-Raman spectroscopy. *Analyst* **125,** 251 (2000).
55. Power Diffraction File (PDF) 00-041-1475 (International Centre for Diffraction Data; Newtown Square, PA).
56. J. Balmain, B. Hannoyer, and E. Lopez: Fourier transform infrared spectroscopy (FTIR) and x-ray diffraction analyses of mineral and organic matrix during heating of mother of pearl (nacre) from the shell of the mollusc *Pinctada maxima. J. Biomed. Mater. Res.* **48**(5), 749 (1999).
57. Q.L. Feng, X.W. Su, F.Z. Cui, and H.D. Li: Crystallographic orientation domains of flat tablets in nacre. *Biomimetics* **3,** 159 (1995).
58. Q.L. Feng, H.B. Li, F.Z. Cui, H.D. Li, and T.N. Kim: Crystal orientation domains found in the single lamina in nacre of the *Mytilus edulis shell. J. Mater. Sci. Lett.* **18,** 1547 (1999).
59. Q.L. Feng, G. Pu, Y. Pei, F.Z. Cui, H.D. Li, and T.N. Kim: Polymorph and morphology of calcium carbonate crystals induced by proteins extracted from mollusk shell. *J. Cryst. Growth* **216,** 459 (2000).
60. H. Sturges: The choice of a class interval. *J. Am. Statist. Assoc.* **21,** 65 (1926).
61. D.W. Scott: On optimal and data-based histograms. *Biometrika* **66,** 605 (1979).

## APPENDIX: STANDARD CHARACTERIZATION TECHNIQUES

### 1. Ash weight (deorganified nacre)

Samples masses were measured after desiccation in a vacuum chamber at room temperature for 24 h and then again after a subsequent 2 days at 250 °C in vacuum, which presumably removes the majority of the organic component.

The difference was found to be 2.4 ± 0.3 wt%.

### 2. Demineralized nacre weight

Samples masses were measured after 24 h desiccation in a vacuum chamber at room temperature, immersion in a disodium salt ethylenediaminetetraacetic acid aqueous solution (0.5M EDTA) for 10 days (the solution was refreshed every day), and an additional 24 h desiccation in a vacuum chamber at room temperature. After this last step, the mass was found to be 6.4 ± 1.4 wt% of the original sample mass.

### 3. Raman spectroscopy

A Kaiser Hololab 5000R Raman spectrometer was used at 785 nm utilizing coherent continuous wave argon/ion and Ti/S lasers. Fresh nacre showed 4 sharp bands due to the vibration of the carbonate ions at 1085 $cm^{-1}$ (symmetric stretching, $\nu_1$), 852 $cm^{-1}$ (out of plane bending, $\nu_2$), 705 $cm^{-1}$ (in-plane bending, $\nu_4$), 207 $cm^{-1}$, and 154 $cm^{-1}$, characteristic of the aragonite structure.[54]

### 4. XRD

Samples were crushed, using mortar and pestle, to a fine powder that was then analyzed with a Rigaku RU300 18 kW rotating anode x-ray generator coupled with a 250 mm high-resolution Bragg-Brettano diffractometer. The generating voltage was set to 60 kV, the current to 300 mA, the scan speed to 0.014° per second, and an angular range of 8–55°. For fresh nacre, the spectrum showed peaks characteristic of aragonite.[55]

### 5. FTIR[27,56]

A Perkin Elmer 2000 FTIR Spectrometer was scanned at a resolution of 4 $cm^{-1}$ with steps of 1 $cm^{-1}$ and the results are shown in Fig. A1.

#### a. EDTA-demineralized nacre

The broadest band on the FTIR spectrum (Fig. A1, upper spectrum) is located at 3448 $cm^{-1}$ (OH and/or NH stretching modes of the organic matrix components). The 2800–3000 $cm^{-1}$ range is characteristic of the C–H stretching modes and exhibits a small band at 2846 $cm^{-1}$. The material is found to be mainly composed of EDTA-protein complexes as demonstrated by the presence of intense bands at 1591 $cm^{-1}$ (carboxylate groups coordinated asymmetric stretching band) and 1409 $cm^{-1}$ (carboxylate symmetric stretching band). Smaller peaks detected at 1288, 1263, 921, and 850 $cm^{-1}$ are characteristic of sulfate groups, while the 1000–1150 $cm^{-1}$ peaks correspond to the major polysaccharide absorption

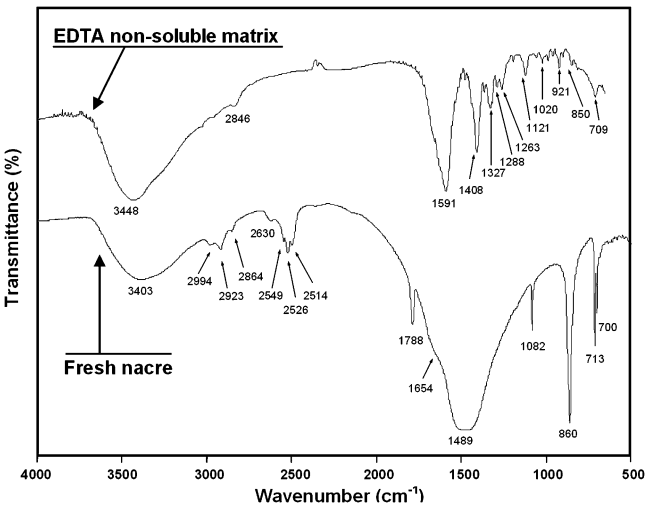


FIG. A1. FTIR spectra of fresh and EDTA-demineralized nacre from *Trochus niloticus*.

region. The presence of bands at 1327 and 709 $cm^{-1}$ indicates amide group absorption (amide III C-N stretching vibration and amide V/VII respectively).

### b. Fresh nacre

Bands are observed in the 3200–3500 $cm^{-1}$ and 2800–3000 $cm^{-1}$ range, as in the spectrum of EDTA-demineralized nacre, and thus attributed to the insoluble organic matrix. Peaks in the 2500–2650 $cm^{-1}$ range (2630, 2549, 2526, and 2514 $cm^{-1}$) correspond to the EDTA soluble organic matrix (OH groups of carboxylic amino acids) and/or carbonate groups ($HCO_2^{3-}$) present in the mineral component, as they do not appear on the EDTA demineralized nacre spectrum. The following wavenumbers peaks were observed that are characteristic of the carbonate ions in aragonite: 713 and 700 ($\nu_4$), 860 ($\nu_2$), 1082 ($\nu_1$), and 1489 $cm^{-1}$. The peak located at 1788 $cm^{-1}$ is related to the C = O groups of the carbonate ions.